Monthly Notices of the ROYAL ASTRONOMICAL SOCIETY

MNRAS **518,** 2921–2937 (2023) https://doi.org/10.1093/mnras/stac3276
Advance Access publication 2022 November 12

Multifilter observations of the complex periodic variations in eight pre-main sequence stars

Chris Koen★

Department of Statistics, University of the Western Cape, Private Bag X17, Bellville, 7535 Cape, South Africa

Accepted 2022 November 7. Received 2022 October 11; in original form 2022 August 4

ABSTRACT

Follow up time series photometry through various combinations of the BVR_CI_C filter set is presented for eight young stars. The complex periodic variability of seven of the stars was first discovered in *TESS* photometry, while one star was first observed by *K2*. The periods of the stars are short – 0.2–0.4 d. Reddening, effective temperatures, and bolometric magnitudes are estimated by fitting spectral energy distributions. The new photometry typically covers several cycles of variability. In some cases, photometry was obtained in more than one observing season. All new light curves differ from those obtained from satellite missions, in some cases substantially so. Amplitudes are almost always larger, the shorter the effective wavelength of the filter, but the relationship can be weak or non-monotonic. Given that all but one of the stars are in associations older than 10 Myr, it seems unlikely that protoplanetary discs play an important role in the complex variability patterns. Modelling of the wavelength dependence of amplitudes in terms of dust absorption in debris discs is explored. The conclusion is that excesses of small grains as compared with the average Galactic composition would be required.

Key words: stars: late type – stars: pre-main-sequence – stars: starspots – stars: variables: other – stars: T Tauri.

1 INTRODUCTION

The advent of extended high-duty cycle time series produced by the *K2* (Howell et al. 2014) and *TESS* (Ricker et al. 2015) missions has led to the discovery of a few dozen late type pre-main sequence stars with very complex patterns of periodic variability (Stauffer et al. 2017, 2018, 2021; Zhan et al. 2019). For convenience, the stars will be referred to as 'CPVs' ('Complex Periodic Variables'), in what follows. The phase folded light curves of the CPVs are characterized by truncated Fourier series, with relatively large (sometimes more than 10) terms; it is this property which sets these objects apart from typical T Tauri stars. Amplitudes are fairly small (a few per cent), and periods short (0.2–0.9 d).

An extensive discussion of CPVs can be found in Stauffer et al. (2017) – see also Stauffer et al. (2018, 2021), Zhan et al. (2019), and Günther et al. (2022); a summary is provided by Koen (2021b). Some key properties taken from these sources are: the stars are young, being members of associations or clusters with ages in the approximate range 1–45 Myr. The one exception is a star in the AB Dor association (age ∼150 Myr). Concomitant with their young ages, spectra generally show Li λ6708 Å absorption and Hα in emission, typical of T Tauri stars. In particular, the equivalent widths of the Hα lines are consistent with the stars being weak-lined T Tauri stars (Stauffer et al. 2017). Spectral types are generally mid-M. As expected, given the spectral types, flares have been observed in some of the stars. Many CPVs have either blue or red excesses, respectively, probably due to hot star-spots and warm dust. Light-curve shapes appear to be stable in some cases, but may also evolve slowly over time-scales of days, or change in the aftermath of flares.

Possible mechanisms driving the variability in CPVs have been proposed by Stauffer et al. (2017), Zhan et al. (2019), Koen (2021a,b), and Günther et al. (2022). Stauffer et al. (2017) ascribed the flux variations to obscuration by a toroid of warm gas clouds at the Keplerian corotation distance from the star; the very high-rotational velocity of the star caused the gas to flow from the stellar equator to the corotation distance. Zhan et al. (2019) pointed out that very narrow features in the light curve require circumstellar material to be at substantial distances from the stellar surface. At such large distances, magnetic fields may be too weak to constrain the gas. Further criticism of the model can be found in Günther et al. (2022).

An alternative hybrid model, incorporating star-spots and a dusty circumstellar disc, is due to Zhan et al. (2019). The disc is assumed to be inclined with respect to the stellar rotation axis, and hence periodically obscures part or all of the star-spots, giving rise to the relatively rapid changes in light level. Günther et al. (2022) note that this model would require a large fraction of rapidly rotating young M dwarfs have discs, and that their rotation and disc axes are misaligned. Observationally, however, debris discs in M dwarf stars are rare (e.g. Matthews et al. 2014), and the existing evidence suggests that such discs are aligned with their stellar rotation axes (Greaves et al. 2014).

It is generally accepted that periodic variability in T Tauri stars is due to the combination of dark star-spots and rotation, but Stauffer et al. (2017) and Zhan et al. (2019) conclude that this mechanism cannot explain CPV light curves. According to these authors, it is either impossible to reproduce light-curve shapes and amplitudes simultaneously, or dark spots alone cannot cause sharp features in CPV light curves. These claims are based on the

★ E-mail: ckoen@uwc.ac.za

Table 1. Basic information about the eight CPVs for which new photometry was obtained. Names based on RA (column 2) are used throughout the paper. Association names and ages (from Gagné et al. 2018) are given in columns 6 and 7. The ($W1 - W2$) colours are from the ALLWISE catalogue (Cutri et al. 2014): assuming that the $W1$ and $W2$ measurements errors are independent, the uncertainty on ($W1 - W2$) is 0.03 mag in all cases. References for the periods in column 5 are: 1) Zhan et al. (2019); 2) Stauffer et al. (2017); 3) Stauffer et al. (2021); 4) this paper. References for the association ages are: 1) Bell et al. (2015); 2) Pecaut & Mamajek (2016).

Name1	Name2	G (mag)	($W1 - W2$) (mag)	P (d)	Ref.	Association	Age (Myr)	Ref.
TIC 425937691	J0021	14.73	0.25	0.4015	4	Tuc Hor	45	1
TIC 206544316	J0113	12.94	0.19	0.3220	1	Tuc Hor	45	1
TIC 435899024	J1252	14.02	0.19	0.36335	3	Lower Cen Crux	15	2
TIC 243381460	J1340	13.33	0.18	0.3684	3	Upper Cen Lup	16	2
TIC 121840452	J1505	14.02	0.22	0.3787	3	Upper Cen Lup	16	2
EPIC 204897050	J1601	15.62	0.27	0.2639	2	Upper Sco	10	2
TIC 289840926	J2110	14.85	–	0.1992	1	Beta Pic moving group	24	1
TIC 332517282	J2323	14.70	0.19	0.4025	1	AB Dor moving group	150	1

Table 2. The estimated interstellar dust absorption, effective temperature, gravity, and bolometric magnitude (columns 2–5) were derived by SED fitting, as described in the text. The last column gives the number of standardized photometric measurements used in the estimation. Standard errors, estimated by bootstrapping, are given in brackets. The column headed 'Sp.' is a spectral type estimated by comparing $T_{\rm eff}$ to entries in table 6 of Pecaut & Mamajek (2013). $\Delta M_{\rm bol}$ is the difference between $M_{\rm bol}$ in column 8, and the bolometric magnitude of a main sequence star of the same spectral type.

Name	$A_{\rm V}$ (mag)	$T_{\rm eff}$ (K)	$\log g$ (dex)	$M_{\rm bol}$ (mag)	$\Delta M_{\rm bol}$ (mag)	Sp.	n
J0021	0.21(0.14)	2860(27)	4.6(0.2)	9.80(0.04)	1.2	M5	13
J0113	0(0)	3160(11)	4.5(0.2)	8.67(0.01)	1.4	M4	15
J1252	0.31(0.13)	3210(55)	3.8(0.2)	7.49(0.04)	2.3	M3.5	13
J1340	0(0)	3200(15)	4.6(0.1)	6.63(0.03)	3.5	M4	19
J1505	0.18(0.15)	3145(46)	4.6(0.2)	7.34(0.06)	2.8	M4	18
J1601	1.0(0.1)	3025(36)	4.0(0.3)	7.87(0.04)	2.9	M4.5	17
J2110	0.09(0.15)	2855(27)	4.8(0.2)	10.13(0.06)	0.9	M5	15
J2323	0.015(0.06)	2985(17)	4.5(0.2)	10.46(0.02)	0.3	M4.5	18

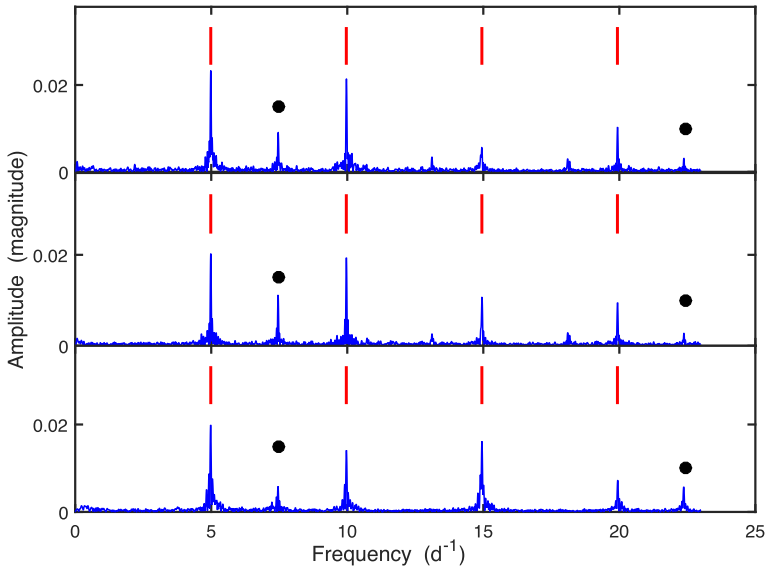

Figure 1. Amplitude spectra of the *TESS* photometry of J0021 obtained during sectors 1 (top), 2 (middle), and 28 (bottom). The short vertical lines indicates multiples of $f_1 = 4.983\,{\rm d}^{-1}$, while the dots are at $1.5f_1$ and $4.5f_1$.

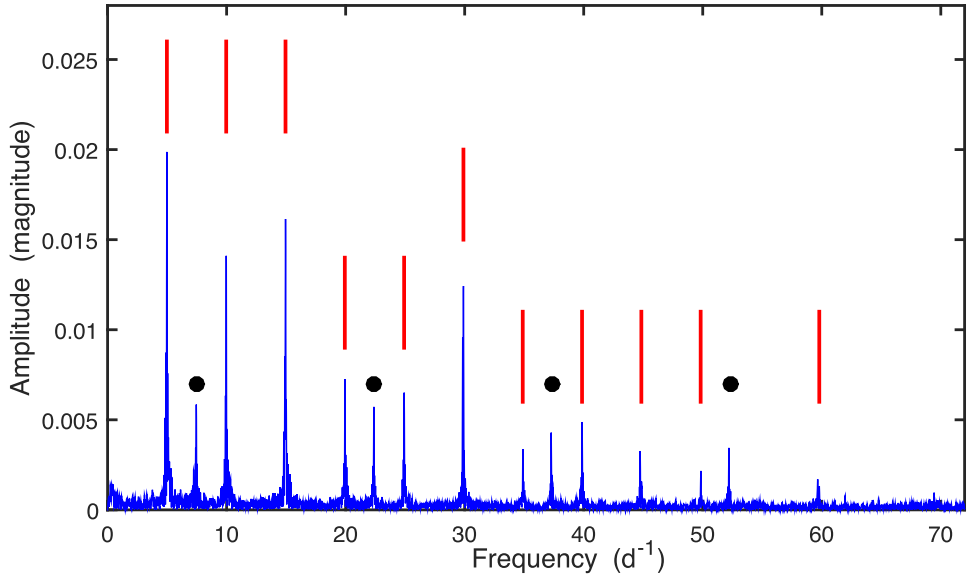

Figure 2. An amplitude spectrum of the *TESS* sector 28 observations of J0021. The short vertical lines indicates multiples of $f_1 = 4.983$ d^{-1}, while the dots are at frequencies $kf_1/2$, where k is uneven.

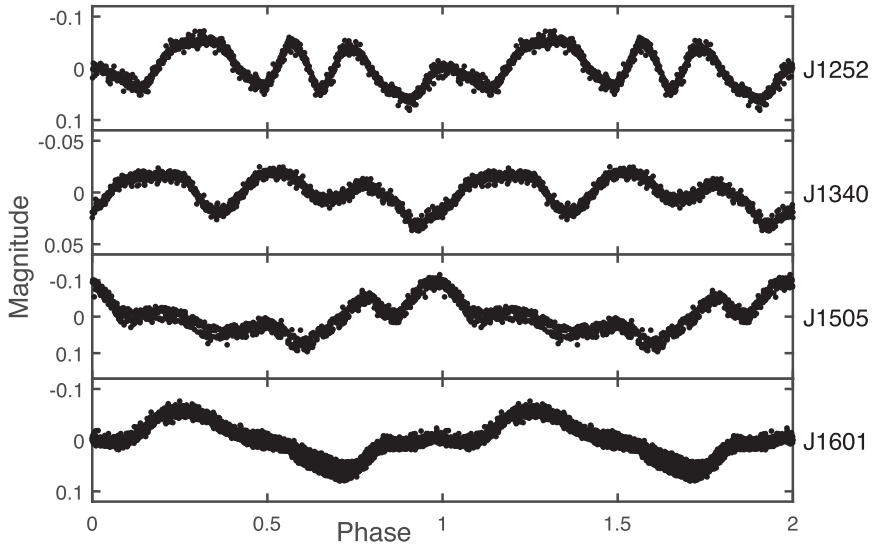

Figure 3. Phase folded *TESS* photometry of J1252, J1340, and J1505, and *K2* photometry of J1601.

conventional modelling approach, in which there are a few circular spots distributed across the stellar surface. However, Koen (2021b) was able to reproduce BVR_CI_C light curves of the CPV RIK 90 to high accuracy with a conventional six spot model. Furthermore, Koen (2021a) found that almost all CPV *TESS* light curves could described by the effects of many small-scale dark features on the stellar surfaces. Koen (2021b) furthermore showed that a number of *K2* CPV light curves can be modelled by mixtures of large circular cool and hot surface spots. Note in this regard that there is support in the literature for the presence of bright spots on late type stars with magnetic fields (Walkowicz & Hawley 2009; Rice, Strassmeier & Kopf 2011; Donati et al. 2014; Koen 2015; Morris et al. 2018; Froebrich et al. 2020).

It is evident from the results presented by Koen (2021b) that multicolour light-curves constrain models – or at least star-spot models – far more than observations obtained through a single filter. The photometry presented in this paper was obtained with this premise in mind, in anticipation of the development of suitable analysis methodology. As far as the author is aware, the only published multifilter photometry of CPVs are the *BVRI* light curves of RIK 90 (Koen 2021b), and observations of four stars by Günther et al. (2022). The latter authors covered one complete cycle of one star, and partial cycles of three other objects, in various combinations of the *griz* filter set. Below, full cycles of variation of eight target stars are presented, mostly observed in VR_CI_C or BVR_CI_C. Some targets were observed in multiple seasons, shedding further light on the time evolution of the light curves.

2 SAMPLE AND BASIC PROPERTIES

Basic information about the target CPVs is summarized in Table 1. In order to avoid the unwieldy TIC numbers of the stars, abbreviated

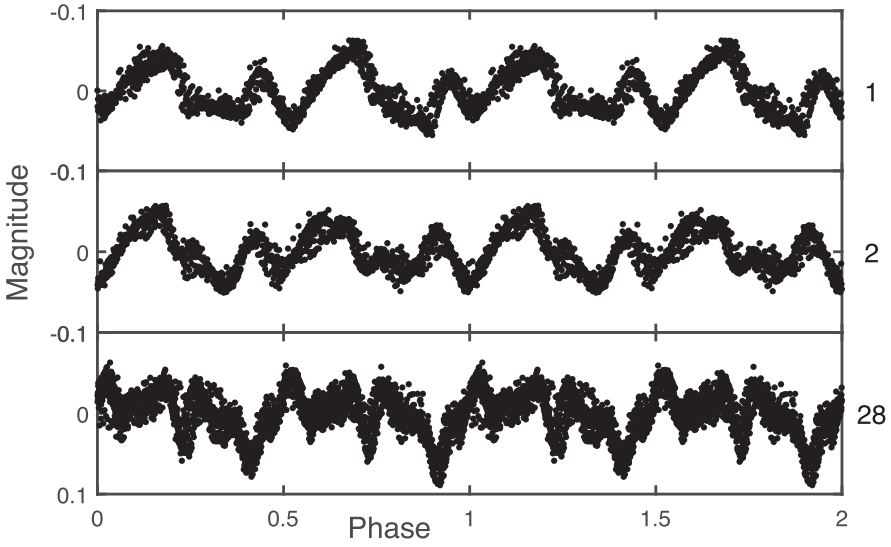

Figure 4. Phase folded *TESS* photometry of J0021. The assumed period is 0.4015 d, i.e. twice the published value. Panels are labelled with the observation sector.

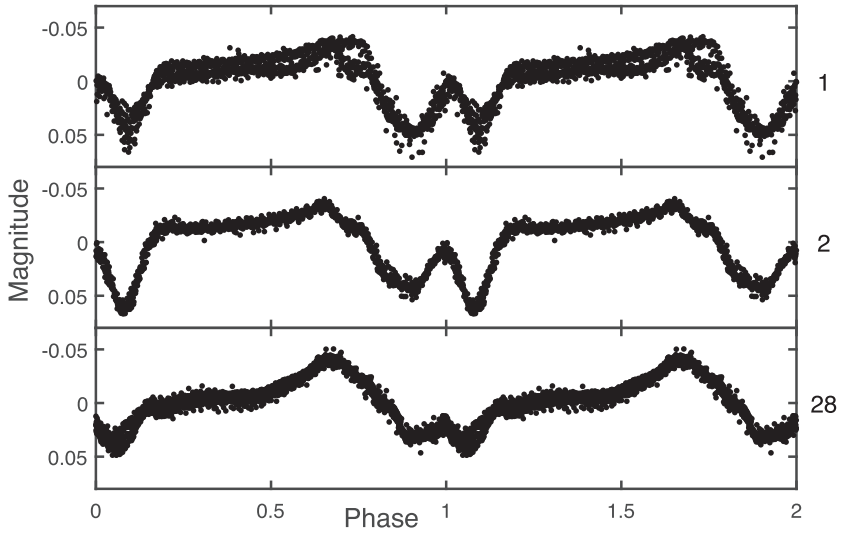

Figure 5. Phase folded *TESS* photometry of J0113. Panels are labelled with the observation sector.

designations based on their Right Ascensions are introduced in column 2 of the Table. The online BANYAN[1] tool (Gagné et al. 2018) was used to determine the most probable membership associations of the stars. Ages of the associations are also given.

Table 2 contains some physical properties derived from published photometry and *Gaia* parallaxes. The photometry and parallaxes were downloaded from VizieR service[2] of the Strasbourg astronomical Data Center. Original sources of the data are APASS ('AAVSO Photometric All-Sky Survey', Henden et al. 2015), *Gaia* (Gaia collaboration 2021), Pan-STARRS ('The Panoramic Survey Telescope and Rapid Response System', Chambers et al. 2016), the 'SkyMapper Southern Survey' (Wolf et al. 2018), 2MASS ('Two Micron All-Sky Survey', Skrutskie et al. 2006), and WISE ('Wide-field Infrared Survey Explorer', Cutri et al. 2014). The efforts of these surveys are gratefully acknowledged.

[1]http://www.exoplanetes.umontreal.ca/banyan/
[2]https://vizier.cds.unistra.fr/viz-bin/VizieR

Dust absorption A_V, effective temperature $T_{\rm eff}$, gravity $\log g$, and bolometric magnitude $M_{\rm bol}$ for each star were estimated by effectively fitting spectral energy distributions (SEDs) to the photometry. This was done by minimizing the sum of squares

$$SS = \sum_{\lambda}^{N_\lambda} \left[M_{\rm bol} - \widehat{M}_{{\rm bol},\lambda} \right]^2$$
$$= \sum_{\lambda}^{N_\lambda} \left\{ M_{\rm bol} - [(m_\lambda + 5 + 5\log_{10} p) - A_V f_\lambda + BC_\lambda)] \right\}^2, \quad (1)$$

where λ is wavelength; m_λ are the photometric measurements; A_V and f_λ, respectively, the V-filter absorption and the extinction law; $M_{\rm bol}$ and BC_λ the bolometric magnitude and bolometric correction; and p the parallax. The notation $\widehat{M}_{{\rm bol},\lambda}$ indicates the bolometric magnitude estimated from the measurement through the filter with effective wavelength λ. The extinction $f_\lambda = A_\lambda/A_V$ was taken from Schlafly et al. (2016), and bolometric corrections (Choi et al. 2016) from the

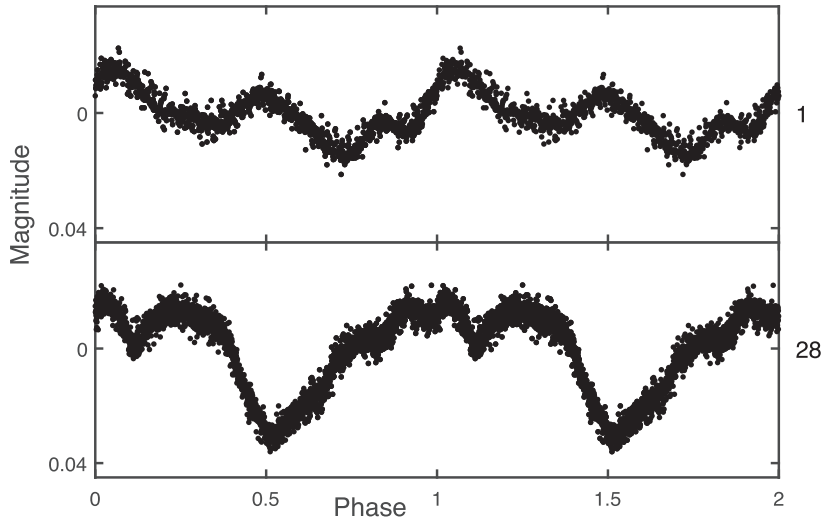

Figure 6. Phase folded *TESS* photometry of J2110. Panels are labelled with the observation sector. Note that observations have been prewhitened by the secondary period $P_2 = 0.6502$ d.

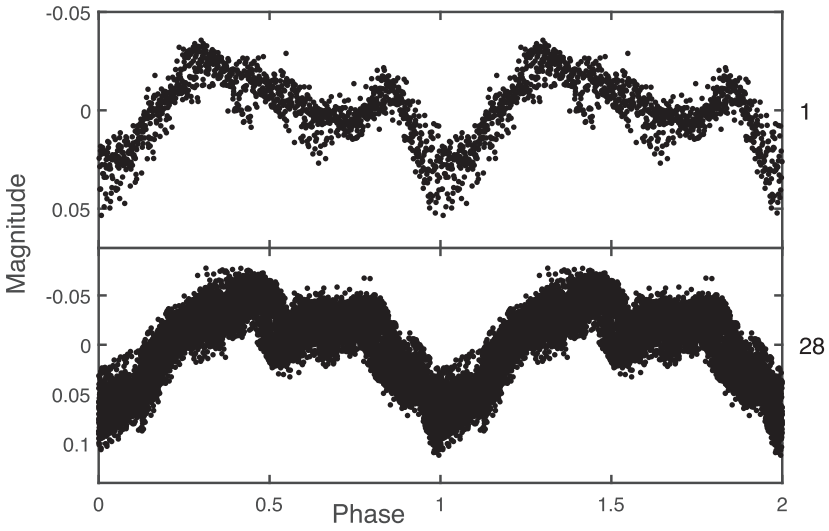

Figure 7. Phase folded *TESS* photometry of J2323. Panels are labelled with the observation sector.

'MESA Isochrones and Stellar Tracks' website.[3] Formal standard errors of the estimates were calculated by bootstrapping – see Koen (2022) for details.

Table 2 also shows rough spectral classifications estimated by interpolating in the spectral type – effective temperature tabulation for pre-main sequence stars by Pecaut & Mamajek (2013; their table 6). The classifications were then used to find the differences between $M_{\rm bol}$ values in column 5 of Table 2, and bolometric magnitudes of main sequence dwarfs of the same spectral types, by comparison with the tabulation by Pecaut, Mamajek & Bubar (2012).[4]

As expected (e.g. Koen 2021b, Günther et al. 2022), the CPVs are more luminous than their main sequence counterparts. The considerable range in $\Delta M_{\rm bol}$ – from 0.23 to 3.5 mag – is noteworthy.

[3]http://waps.cfa.harvard.edu/MIST/model_grids.html#bolometric
[4]http://www.pas.rochester.edu/~emamajek/EEM_dwarf_UBVIJHK_colors_Teff.txt

Mid-infrared photometry of four of the stars (J1252, J1340, J1505, and J1601) were scrutinized by Luhman (2022) for excesses pointing to the presence of circumstellar discs, with null results. ALLWISE ($W1 - W2$) colours (Cutri et al. 2014) available for three of the remaining stars (see Table 1) are similar to those in the Luhman (2022) study, hence it may conclude that there is no overt photometric evidence for circumstellar dust. Three stars were detected by *GALEX* (the 'Galaxy Evolution Explorer' – Martin et al. 2005) in the near-ultraviolet: J1505 (Bianchi et al. 2011), J2110 (Schneider & Shkolnik 2018), and J2323 (Bianchi, Shiao & Thilker 2017). J2110 is also possibly an X-ray source – there was a ROSAT detection 7 arcsec from its position (Voges et al. 1999).

The next section of the paper deals with *TESS* and *K2* observations of the stars. Section 4 contains a brief description of the acquisition of new multicolour photometry. The photometry is discussed in Section 5, and its interpretation in terms of dust absorption in Section 6. A few closing remarks follow in Section 7.

Table 3. The photometric observing log. Numbers of measurements across filters are in the last column.

Starting time (HJD 2450000 +)	Filters	Run length (h)	*N*
	J0021		
9104.4321	*VI*	3.2	46–48
9107.4604	*VI*	3.1	64–66
9502.2455	*RI*	5.7	134–136
9505.2638	*VI*	4.4	57–58
9506.2407	*VI*	5.2	73–84
	J0113		
9447.4763	*VRI*	5.1	101
9448.4525	*BVRI*	5.5	33–94
9451.4305	*BVRI*	6.2	70–73
	J1252		
9360.2045	*VRI*	5.6	104–105
9362.2135	*VRI*	5.7	88–97
9365.1942	*BI*	6.5	107–113
9367.1962	*BI*	3.8	67–68
	J1340		
9357.2528	*BVRI*	6.7	87–103
9358.1993	*BVRI*	8.0	107–114
9361.2093	*VRI*	2.9	35–40
	J1505		
9359.2582	*VRI*	6.7	71–77
9766.2072	*VRI*	6.6	43–150
9767.2064	*VRI*	3.7	52–58
	J1601		
8626.3609	*BVRI*	6.6	29–52
8627.3765	*BVRI*	6.4	39–45
	J2110		
9104.2302	*VI*	2.4	35–42
9107.2419	*VI*	3.4	60–63
9108.2249	*VI*	2.9	50
9357.5418	*VRI*	3.5	51–54
9358.5399	*VRI*	3.7	55–57
9442.3543	*R*	5.0	279
	J2323		
9511.2804	*RI*	4.2	96–97
9512.2693	*RI*	5.4	129

3 SATELLITE DATA

The stars J1252, J1340, and J1505 were observed during *TESS* sector 11. The KSPSAP (optimal aperture size light curve) photometry of these stars provided by the MIT Quick Look Pipeline (Huang et al. 2020) was downloaded from the *Mikulski Archive for Space Telescopes* (*MAST*).[5] KSPSAP reductions were also used for J0113 (observed during sectors 1, 2, and 28). J2110 and J0021 were observed, respectively, twice (sectors 1 and 28) and thrice (sectors 1, 2, and 28). For these two objects, 'Pre-search data conditioned simple aperture photometry' (PDCSAP) provided by the Science Processing Operations Center (Jenkins et al. 2016) was also obtained from *MAST*. For J2323 KSPSAP (sector 2) and PDCSAP (sector 29), light curves were downloaded. In the case of J1601, *K2* (Howell et al. 2014) photometry was downloaded from the NASA Exoplanet Archive.[6]

A few grossly outlying points were removed. Light curves were detrended by low-order polynomials in order to remove obvious instrumental artefacts. In all cases except for J2110 and J0021, a single frequency and a number of its harmonics were fitted to the data. Observations deviating from the fitted light curve by more than 3σ were discarded.

As noted by Zhan et al. (2019), J2110 has an obvious secondary period $P_2 = 0.65025$ d, which is harmonically unrelated to the base period of the complex variations – presumably due to rotational modulation of the light from a companion star. The data for this star were, therefore, pre-whitened by a sinusoid with frequency $1/P_2$ and amplitude determined as part of the fitting procedure. The amplitudes associated with P_2 were 0.015 mag (sector 1) and 0.011 mag (sector 28).

The case of J0021 is somewhat unusual. Zhan et al. (2019) quote a single period $P_1 = 0.2007$ d (frequency $f_1 = 4.983\,\mathrm{d}^{-1}$) for this star. Fig. 1 shows amplitude spectra of the light curves from each of the three sectors; it is noteworthy that there is power not only at harmonics of f_1 but also at $1.5f_1$ and $4.5f_1$. The cadences of the first two sectors observed (1 and 2) were 30 min, giving a Nyquist frequency of $24\,\mathrm{d}^{-1}$. The last of the three sectors, 28, was monitored at 10 min cadence, i.e. the Nyquist frequency is $72\,\mathrm{d}^{-1}$. This larger frequency range allows further clarification of the situation – see Fig. 2, which shows four harmonics of $f_1/2$, which are *not* harmonics of f_1. The implication is that the base frequency is likely to be $f_1/2$, and not f_1, i.e. the true period is probably $2P_1 = 0.4015$ d.

If the period of J0021 is indeed 0.4015 d, then one cycle of variability consists of two near identical half cycles. This would be an important clue as to the mechanism responsible – in particular, it seems unlikely that orbiting clouds of dust could produce the effect. On the other hand, similar complex star-spot patterns on two hemispheres of the star could reproduce these observations – see also Koen (2021a). In what follows, it is assumed that the correct period is 0.4015 d.

Phase-folded photometry of the three stars with single sectors of *TESS* observations, and the single star observed by *K2*, are plotted in Fig. 3. Phased light curves of the remaining stars are in Figs 4–7. The latter figures, which contain replicated light curves, offer the opportunity to study the evolution of the variability. In particular, the end of sector 1 and start of sector 28 were 1.94 yr apart (1.86 yr between sectors 2 and 28). Examination of the figures show very little change between patterns of variability from successive sectors, but noticeable (J0113, J2323) to substantial (J0021, J2121) changes between widely separated runs. Note also the small, but notable differences between the first and second halves of the cycles in J0021, underscoring the information in Figs 1 and 2.

4 SAAO OBSERVATIONS

All new measurements were made at the Sutherland site of the South African Astronomical Observatory (SAAO), using the equipment and observing methodology described in Koen (2022). Contemporaneous photometry through various combinations of the *VRI* filter set was obtained for most stars. Four of the stars were also monitored in *B*, while J2323 was only observed in *R* and *I*. (Note that the latter two filters have Cousins transmissions; the subscripts '*C*' are omitted for convenience). The observing log is given in Table 3.

5 RESULTS

Koen (2021b) used photometry of RIK 90 to demonstrate that light curves obtained through different filters are close to being scaled versions of each other, with the amplitude increasing with decreasing wavelength. Effectively this means that there is a linear relationship

[5] https://mast.stsci.edu/portal/Mashup/Clients/Mast/Portal.html
[6] https://exoplanetarchive.ipac.caltech.edu/

Table 4. Slopes obtained when regressing photometry through other filters on the *I* filter photometry. Numbers in brackets are the (one sigma) uncertainties in the slope estimates.

Star	J0113	J1252	J1340	J1505	J1601	J2110	J2323	J0021
a_R	1.19(0.03)	1.43(0.04)	1.03(0.03)	1.40(0.04)	1.10(0.05)	1.49(0.04)	1.46(0.11)	1.31(0.04)
a_V	1.33(0.03)	1.59(0.05)	1.03(0.04)	1.78(0.12)	1.23(0.08)	1.75(0.04)	–	1.44(0.07)
a_B	–	1.32(0.04)	1.16(0.06)	–	1.61(0.18)	–	–	–

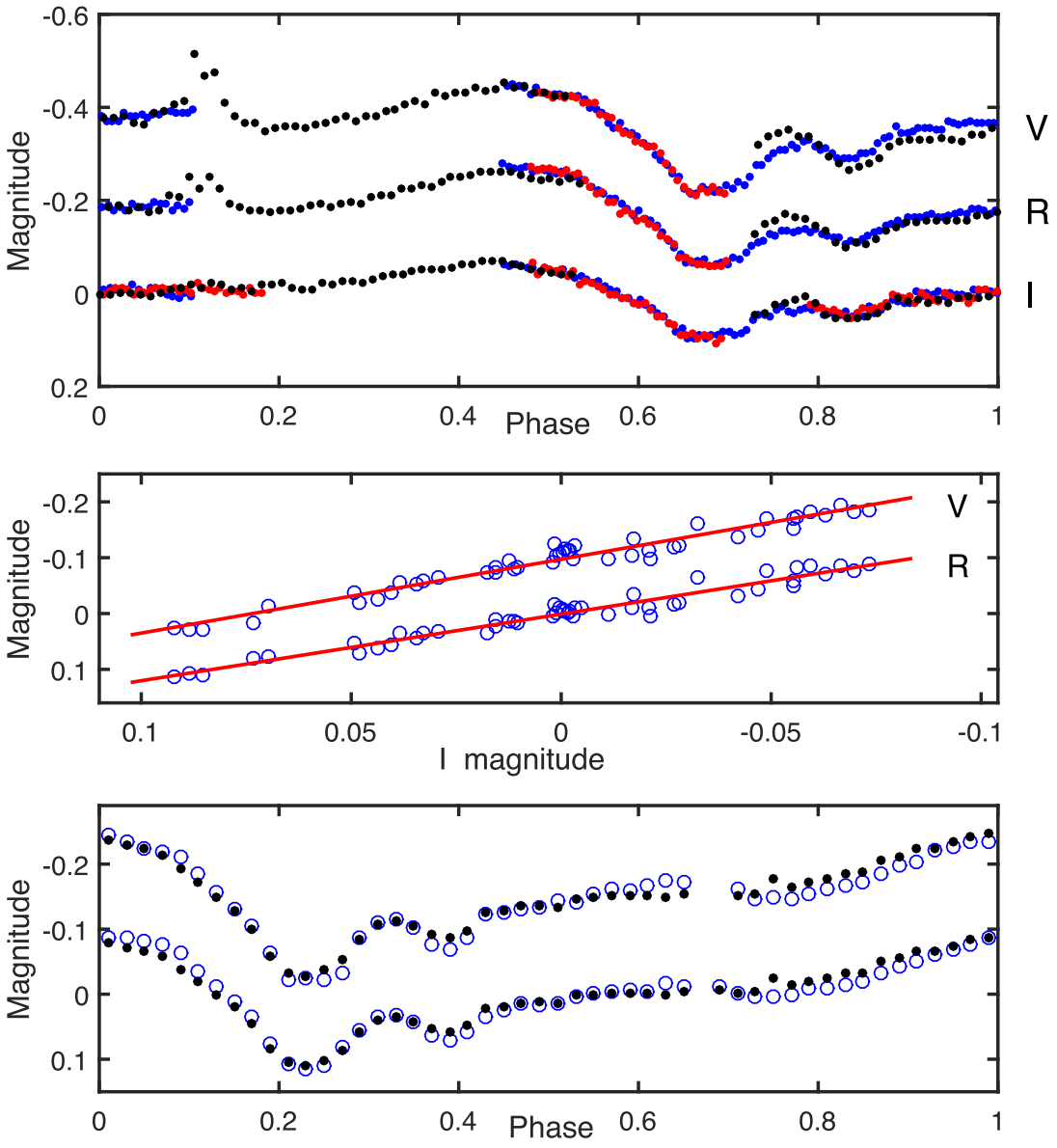

Figure 8. Top panel: Phase folded SAAO observations of J0113. The light-curve magnitude zero-points are arbitrary. Different coloured dots denote data from different nights. Middle panel: The relation between *V* and *I*, and between *R* and *I*, for J0113. The lines are linear regression fits. Magnitude zero-points are arbitrary. Bottom panel: Open circles denote binned *V* (top) and *R* (bottom) phased light curves of J0113. The dots show scaled binned *I* filter photometry. The scale factors used are the slopes of the lines in the middle panel.

between magnitudes measured through different filters – a common occurrence for weak-lines T Tauri stars (Koen 2016).

Given the late spectral types of the CPVs, the stars are brightest in the *I* band, and therefore the *I* filter photometry will be used as baseline. Formally,

$$m_\lambda = a_\lambda m_I + \text{error} \quad (2)$$

where λ indexes the relevant filter (*B*, *V*, or *R*), and m_λ is the mean-subtracted magnitude measured through filter λ. In order to regress photometry though other filters on the *I* filter observations, it is required that all values refer to the same phase of variability. There are a number of ways in which this can be done; perhaps the easiest is to subdivide the [0,1] phase interval into equally spaced bins, and to use the bin averages for each of the filters. Flare events are edited

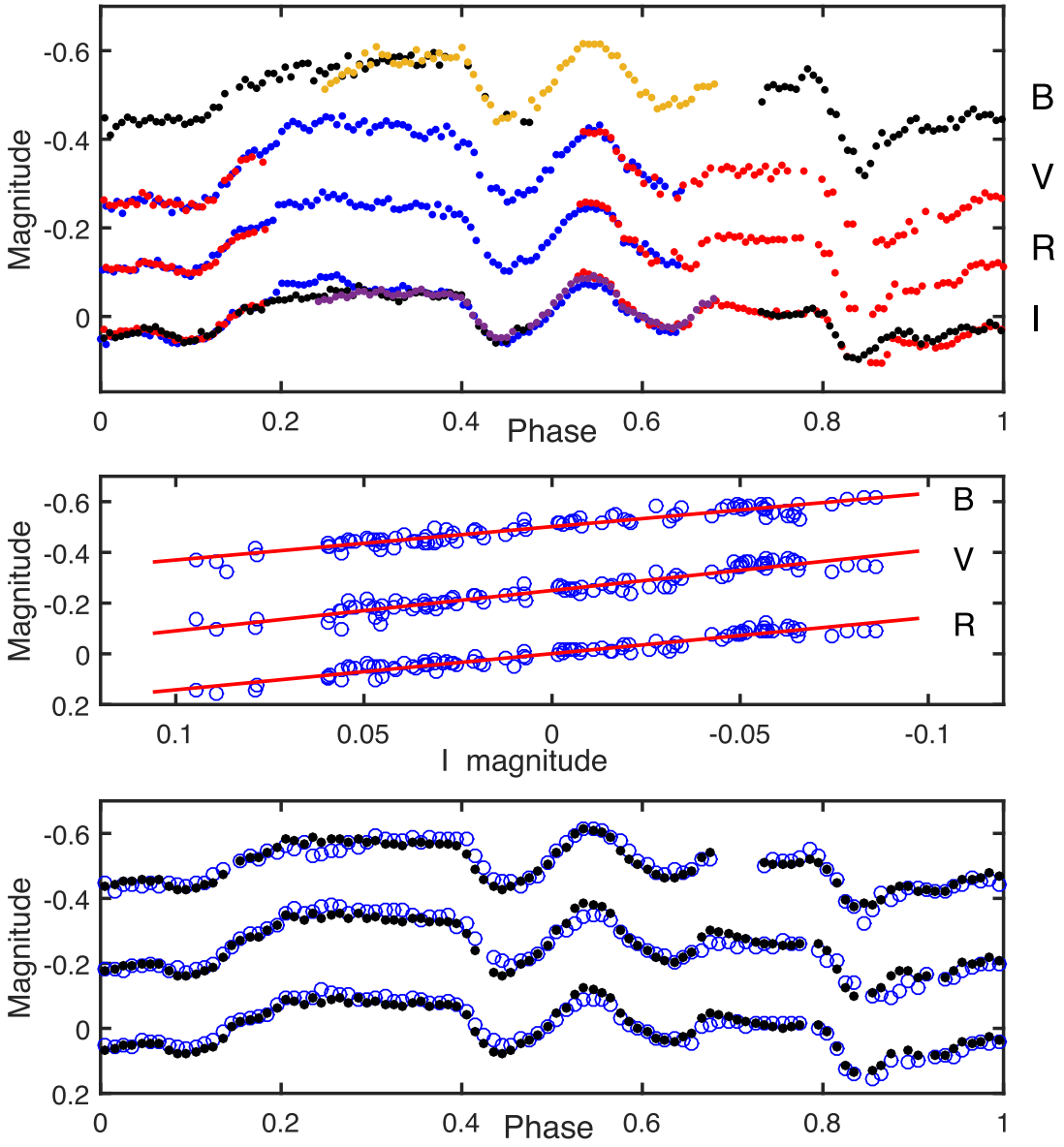

Figure 9. Top panel: Phase folded SAAO observations of J1252. The light-curve magnitude zero-points are arbitrary. Different coloured dots denote data from different nights. Middle panel: The relation between *B* and *I*, *V* and *I*, and *R* and *I*, for J1252. The lines are linear regression fits. Magnitude zero-points are arbitrary. Bottom panel: Open circles denote binned *B* (top), *V* (middle), and *R* (bottom) phased light curves of J1252. The dots show scaled binned *I* filter photometry. The scale factors used are the slopes of the lines in the middle panel.

from the light curves for the analyses, since these are atypical and could bias the results.

The estimated regression slopes a_λ are given in Table 4.

5.1 J0113

A spectral classification is available – M3.7 (Kraus et al. 2014); this can be compared to the spectral type (M4) in Table 2, derived from the estimated effective temperature.

Although the resolution is poor, two successive flares are visible in the SAAO *V* and *R* light curves (Fig. 8). There are obvious differences between the two light curves from different nights covering phases around 0.8, especially in *V*, despite these being obtained only 4 d apart. The overall shape of the light curve is similar to that in Fig. 5, although the two dips (at phases ∼0.65 and ∼0.85 in Fig. 8) are shallower and have different relative depths.

The middle panel of Fig. 8 illustrates the relations between the *V*, *I* and *R*, *I* photometry, after removing the atypical flare events and binning the data shown in the top panel. Inspection of the bottom panel of the figure shows that the scaled *I* filter photometry gives good overall representations of the measurements through the other filters. Note though that there are systematic differences – see particularly around phases 0.4 and 0.65.

5.2 J1252

There is a marked resemblance between the *TESS* (Fig. 3) and SAAO (Fig. 9) light curves, although the local maximum near phase 0.7 is flat, rather than rounded, in the SAAO observations. Shorter

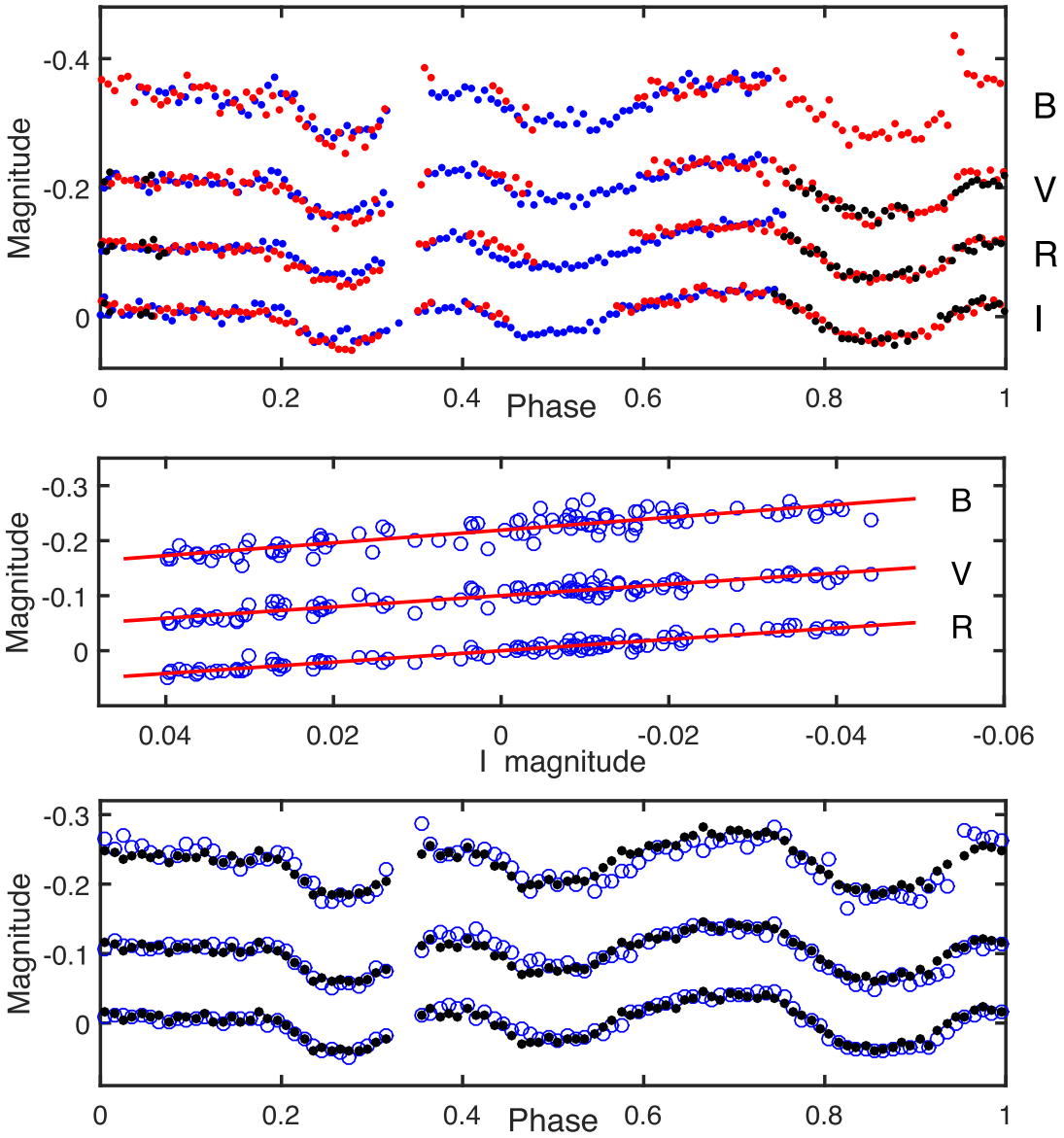

Figure 10. Top panel: Phase folded SAAO observations of J1340. The light-curve magnitude zero-points are arbitrary. Different coloured dots denote data from different nights. Middle panel: The relation between *B* and *I*, *V* and *I*, and *R* and *I*, for J1252. The lines are linear regression fits. Magnitude zero-points are arbitrary. Bottom panel: Open circles denote binned *B* (top), *V* (middle), and *R* (bottom) phased light curves of J1252. The dots show scaled binned *I* filter photometry. The scale factors used are the slopes of the lines in the middle panel.

time-scale variability is visible in the SAAO photometry – see, for example, the differences between photometry from different nights in the *I* filter measurements near phases 0.2–0.3 and 0.85–0.95.

Curiously, the slope a_B is smaller that both a_R and a_V (Fig. 9, Table 4). The scaled *I* filter light curve is perhaps most similar to the light curve in *B*; $a_V * I$ and $a_R * I$ differ systematically from *V* and *R* in the sinusoidal variation at phase ∼0.45–0.65 (Fig. 9, bottom panel).

5.3 J1340

The star is considerably brighter than an M4 main sequence star ($\Delta M_{bol} = 3.4$ mag). The SAAO light curve (Fig. 10) is similar to that obtained by *TESS*. A flare is visible in the *B* filter photometry (near phase 0.95). There appears to be a concomitant enhancement in the *V* filter flux from the particular night, but none in *R* and *I*.

The slopes a_R and a_V are very shallow, not significantly different from unity (Table 4, Fig. 10 middle panel). The *B*–*I* regression slope is also relatively small, only marginally significantly larger than unity.

5.4 J1505

Only the part of the *TESS* light curve (Fig. 3) around the global maximum appears to have a similarly shaped counterpart in the SAAO observations (top panel of Fig. 11, phase ∼0.82). Note in particular that the *TESS* light curve has four maxima per cycle, while the SAAO light curve has six. Fig. 12 is a direct comparison of the two light curves, and also includes *I* filter observations obtained on JD 2459359. It is interesting that the relatively narrow light maximum appears to be the only feature which is consistently present. Given

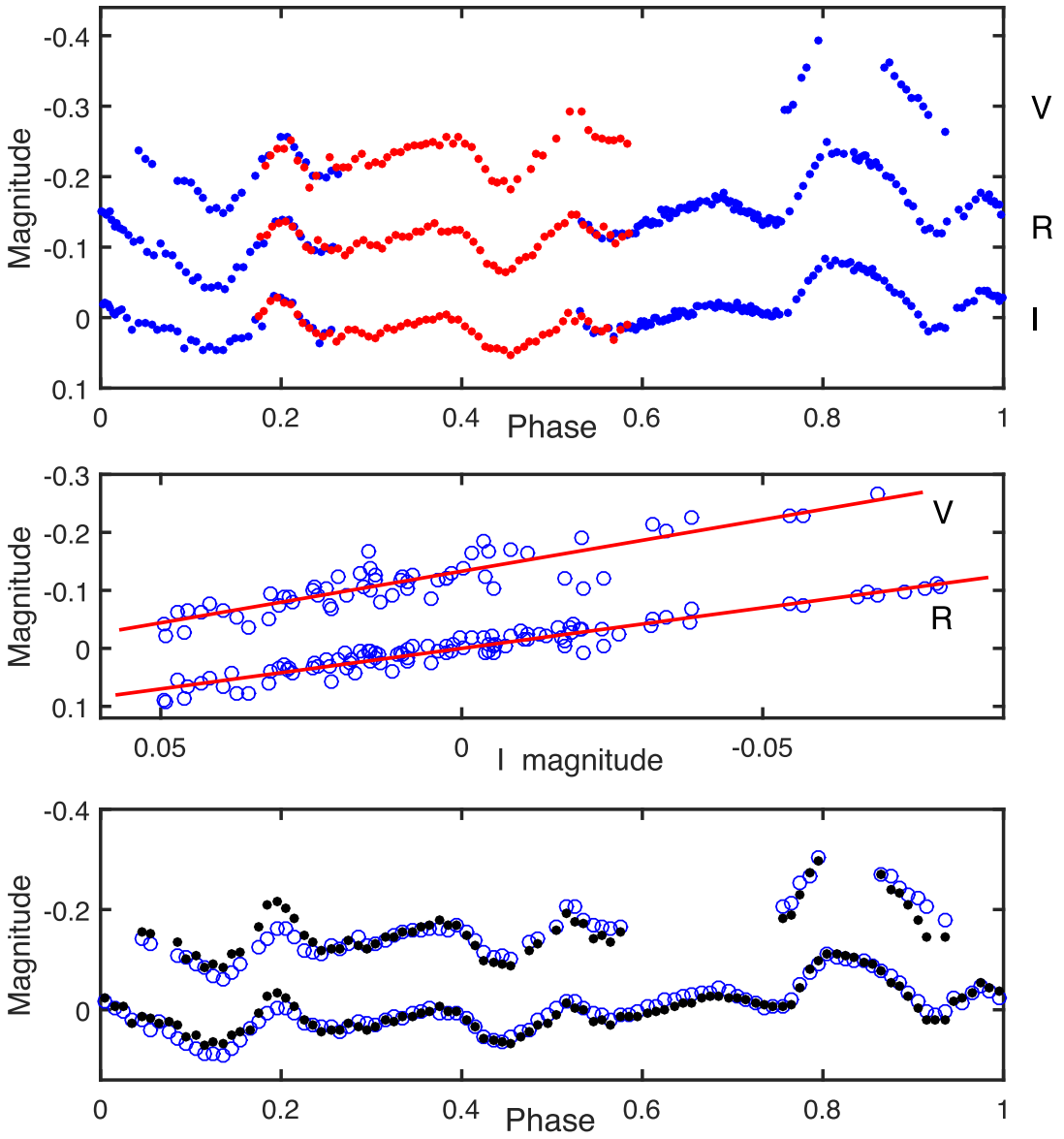

Figure 11. Phase folded SAAO observations of J1505. The light-curve magnitude zero-points are arbitrary. Different coloured dots denote data from different nights. Note that the data from JD 2459359 (see Table 3) were not used as it could not be satisfactorily phased with the observations from the other two nights. Middle panel: The relation between *V* and *I*, and between *R* and *I*, for J1505. The lines are linear regression fits. Magnitude zero-points are arbitrary. Bottom panel: Open circles denote binned *V* (top) and *R* (bottom) phased light curves of J1505. The dots show scaled binned *I* filter photometry. The scale factors used are the slopes of the lines in the middle panel.

the *GALEX* detection of the star (Bianchi et al. 2011), it is tempting to ascribe this light maximum to an accretion hot spot.

Linear magnitude–magnitude regressions are plotted in the middle panel of Fig. 11, and scaled phased *I* filter photometry is compared to the *R* and *V* photometry in the bottom panel.

5.5 J1601

Also known as USco CTIO 56. The star was classified M5 by Ardila, Martin & Basri (2000). The effective temperature in Table 2 corresponds to an M4 young dwarf (Pecaut & Mamajek 2013, table 6).

Both the *K2* (Fig. 3) and SAAO (Fig. 13) light curves are relatively smooth, but there is no strong resemblance. The scaled *I* light curves is compared to its *BVR* counterparts in the bottom panel of Fig. 13; the agreements in *V* and *R* are remarkably good, while the *B* filter light curve is perhaps too noisy to draw any strong conclusions.

5.6 J2110

The effective temperature in Table 2 is consistent with the M5 classification by Riaz, Gizis & Harvin (2006).

The *TESS* (Fig. 6) and SAAO (Fig. 14) light curves are similar in shape, but differ in the details. The regressions of the *R* and *V* magnitudes on *I* are plotted in the middle panel of Fig. 14. The bottom panel of Fig. 14 shows a mismatch between the scaled *I* magnitudes and *R* near phase 0.1; the origin is obvious in the top

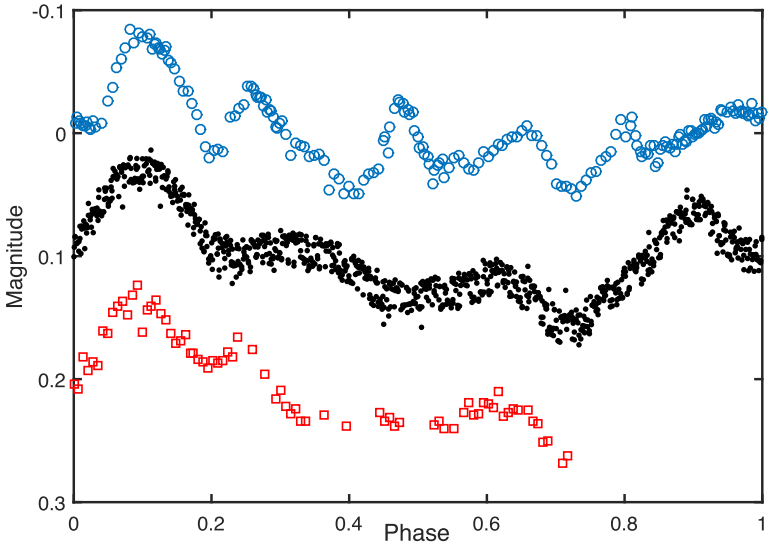

Figure 12. Phased light curves of J1505. From top to bottom: JD 2459766-7 (*I* filter); *TESS* sector 11; JD 2459359 (*I* filter). Magnitude and phase zero-points are arbitrary.

panel of the figure, but may simply be due to the *R* and *I* observation being from different epochs.

5.7 J2323

The bolometric magnitude of J2323 does not differ much from that of a main sequence star of spectral type M4.5.

The SAAO light curve (Fig. 15), although noisy, clearly has a lower amplitude (particularly in *I*) than the *TESS* data. The morphology of the variations is also different. There appears to have been a small flare observed through the *R* filter on one night (see light-curve near phase 0.3).

The relationship between *R* and *I* magnitudes is illustrated in the middle panel of Fig. 15, while the scaled *I* filter light curve is compared to its *R* filter counterpart in the bottom panel.

5.8 J0021

A spectral type of M5.5 was assigned by Kirkpatrick et al. (2011), while the effective temperature in Table 2 is close to that of an M5 PMS star (table 6 of Pecaut & Mamajek 2013).

The morphology of the SAAO light curve of J0021 is very variable (Figs 16, 17) and bears little resemblance to any of the *TESS* light curves (Fig. 4). Note that the JD 2459107 and JD 2459505 light curves have been shifted by half a period, in order to more easily compare these to other observations. It does look as though the symmetry around phase 0.5 visible in Fig. 4 persists in the SAAO photometry, albeit much less pronounced. Because of the changeability in the light curves, no attempt was made to phase photometry from different nights.

Note that the isolated point in the top panel of Fig. 17 at (0.27, 0.36) is part of the *V* filter light curve obtained on JD 2459506, i.e. a ∼0.5 mag flare of very brief duration. A low-amplitude flare is also visible in the JD 2459104 light curve.

Fig. 17 (middle panel) shows the relationships between the *R* and *I* magnitudes measured on JD 2459502, and *V* and *I* magnitudes from JD 2459506 (*V*2). Also shown is the *I*–*V* relationship taking into account data from all nights on which both these filters were used (*V*1). The slopes of the lines marked *V*1 and *V*2 are 1.44 (0.07) and 1.29 (0.11), respectively.

6 INTERPRETATION IN TERMS OF VARIABLE DUST EXTINCTION

In this section of the paper we explore the implications of ascribing the variability of the CPVs entirely to changes in dust obscuration. The discussion closely follows that in Koen (2021b).

If variable dust absorption is solely responsible for the photometric variability, then

$$a_\lambda \propto A_\lambda / A_\mathrm{I}, \tag{3}$$

where the scale factors a_λ are defined in (2), and A_λ is the absorption at wavelength λ. Note that although A_λ changes with time, the constitution of the dust – and hence A_λ/A_I – is assumed constant.

Using equation (3), the scale factors a_λ in Table 4 can be rewritten in terms of ratios of total to selective absorption, $R_\lambda = A_\lambda/E(V-I)$, which allows convenient comparison with standard Galactic dust extinction. The results are plotted in Fig. 18. Excluded are the very uncertain a_B for J1601, and all data for J1340, for which the estimated $E(V-I)$ is extremely small. The plot is split into two panels with different vertical scales in order to display the results more clearly.

Also plotted in Fig. 18 are the extinction 'anchor points' from Fitzpatrick (1999) and average Galactic extinction calculated from Schlafly et al. (2016). For comparison with the stars of this paper, results for the CPV RIK 90 taken from Koen (2021b) are also included.

With the exception of J1252, R_λ increases monotonically with wavenumber. For RIK 90, the dependence of R_λ on wavenumber is very similar to that of Galactic extinction, but for the remainder of the stars it is steeper, i.e. there is an excess of absorption in the blue.

Following work by De Marchi et al. (2016) on extinction in the Tarantula nebula, Koen (2021b) argued that the wavelength dependence of R_λ in RIK 90 could be explained by dust of similar composition as that in the Galaxy. However, the fact that the R_λ values for the star are larger than those seen in the Galaxy requires an additional large-grain component, which provides wavelength-independent absorption in the optical. If this interpretation is correct,

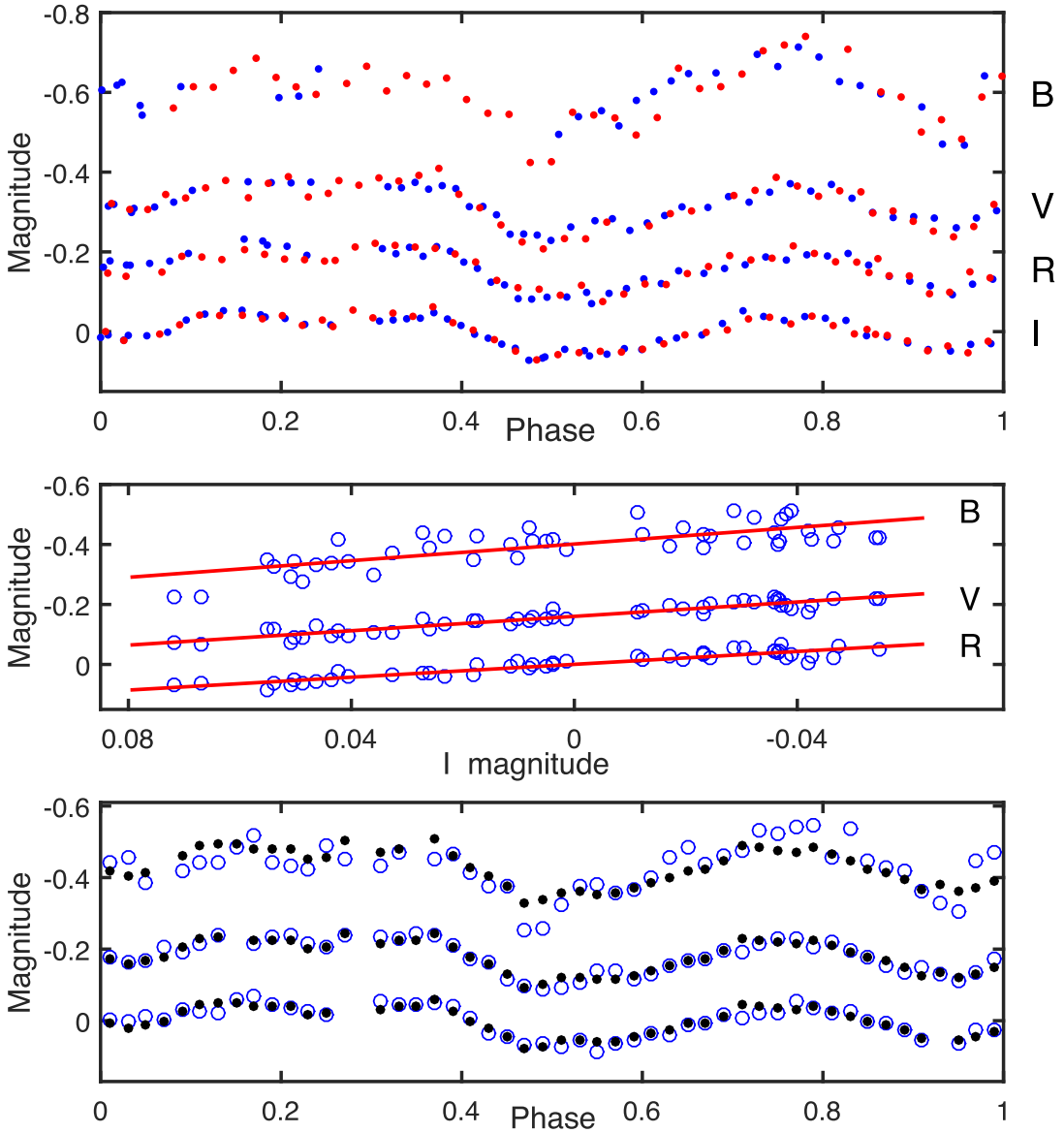

Figure 13. Top panel: Phase folded SAAO observations of J1601. The light-curve magnitude zero-points are arbitrary. Different coloured dots denote data from different nights. Middle panel: The relation between *B* and *I*, *V* and *I*, and *R* and *I*, for J1601. The lines are linear regression fits. Magnitude zero-points are arbitrary. Bottom panel: Open circles denote binned *B* (top), *V* (middle), and *R* (bottom) phased light curves of J1601. The dots show scaled binned *I* filter photometry. The scale factors used are the slopes of the lines in the middle panel.

then J1252 aside, the CPVs of this paper have excesses of small grains over the Galactic grain distributions, leading to increased absorption in the blue.

7 CONCLUDING REMARKS

Perhaps the most important conclusion of this study is that CPVs do not have a homogeneous set of variability properties. In particular, stability of the light curves and amplitudes as function of wavelength vary from star to star.

The marked changes in the light-curve shapes of some of the stars discussed in this paper are in stark contrast with the observation of Günther et al. (2022) that, over time-scales of the order of a year '. . . the major features of the complex rotators remain unchanged. . . '. In particular, see the collection of light curves of J0021 in Figs 16 and 17.

The changes in *TESS* light-curve morphologies of J0021 (Fig. 4) and J2110 (Fig. 6) pose a challenge for any model involving co-rotating circumstellar dust, or a tilted dusty disc. For example, if the sharp dips near phases 0.45 and 0.85 in the sector 28 photometry of J0021 are due to dust, it would need to be explained why these are absent from the light curves from earlier sectors.

According to Padgett et al. (2006), Cieza et al. (2007), and references therein, protoplanetary discs in weak-lined T Tauri stars are rare, and not detected in stars older than about 10 Myr (see also the recent study by Mendigutía et al. 2022). Given that only J1601 has an age of this order (Table 1), and that three of the CPVs have ages in excess of 40 Myr, it appears unlikely that protoplanetary discs play an important role in the variability of these stars. Furthermore, very few debris discs have been detected in M dwarfs generally (Matthews et al. 2014; Hughes, Duchêne & Matthews 2018).

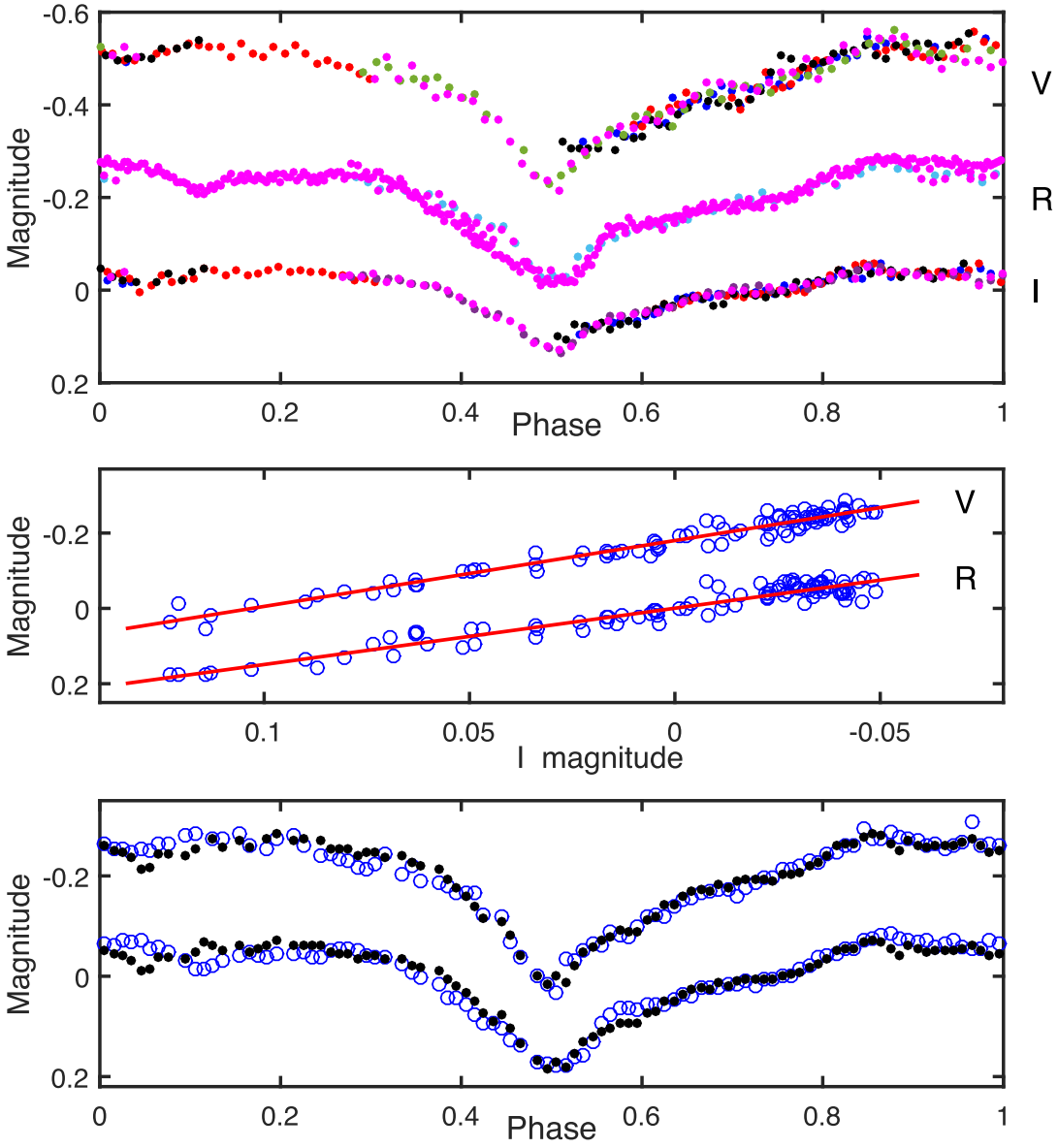

Figure 14. Top panel: Phase folded SAAO observations of J2110. The light-curve magnitude zero-points are arbitrary. Different coloured dots denote data from different nights. Middle panel: The relation between *V* and *I*, and between *R* and *I*, for J2110. The lines are linear regression fits. Magnitude zero-points are arbitrary. Bottom panel: Open circles denote binned *V* (top) and *R* (bottom) phased light curves of J2110. The dots show scaled binned *I* filter photometry. The scale factors used are the slopes of the lines in the middle panel.

There is considerable variability in the magnitude–magnitude slopes summarized in Table 4. For J1340, a_R and a_V do not differ significantly from unity, and $a_B = 1.16$ is also quite small. On the other hand, for J2110, $a_V = 1.75$ is much larger than corresponding slopes for other stars. For J1252, a_B is smaller than both a_V and a_R. There is no obvious correlation with any of the properties in Table 2.

Although quite complex, the *TESS* light curves of J0021 in Fig. 4 are very similar over the two halves comprising a full cycle of variability. It seems unlikely that a tilted dusty disc could play an important role in producing this effect. On the other hand, the occurrence of similar star-spot patterns on the two hemispheres of the star does not seem far fetched. Furthermore, given that the amplitude dependence on wavelength of J0021 (Fig. 18) is similar to that of several of the other stars studied in this paper, it is tempting to assume similar variability mechanisms at play.

For the four stars for which spectral types are available from the literature, the classifications via effective temperatures derived from SED fitting are closely similar to those from spectroscopy.

ACKNOWLEDGEMENTS

Allocation of telescope time by the South African Astronomical Observatory, and the smooth operation of the equipment, are gratefully acknowledged. The research made use of the VizieR catalogue maintained by the 'Centre de Données astronomiques de Strasbourg'.

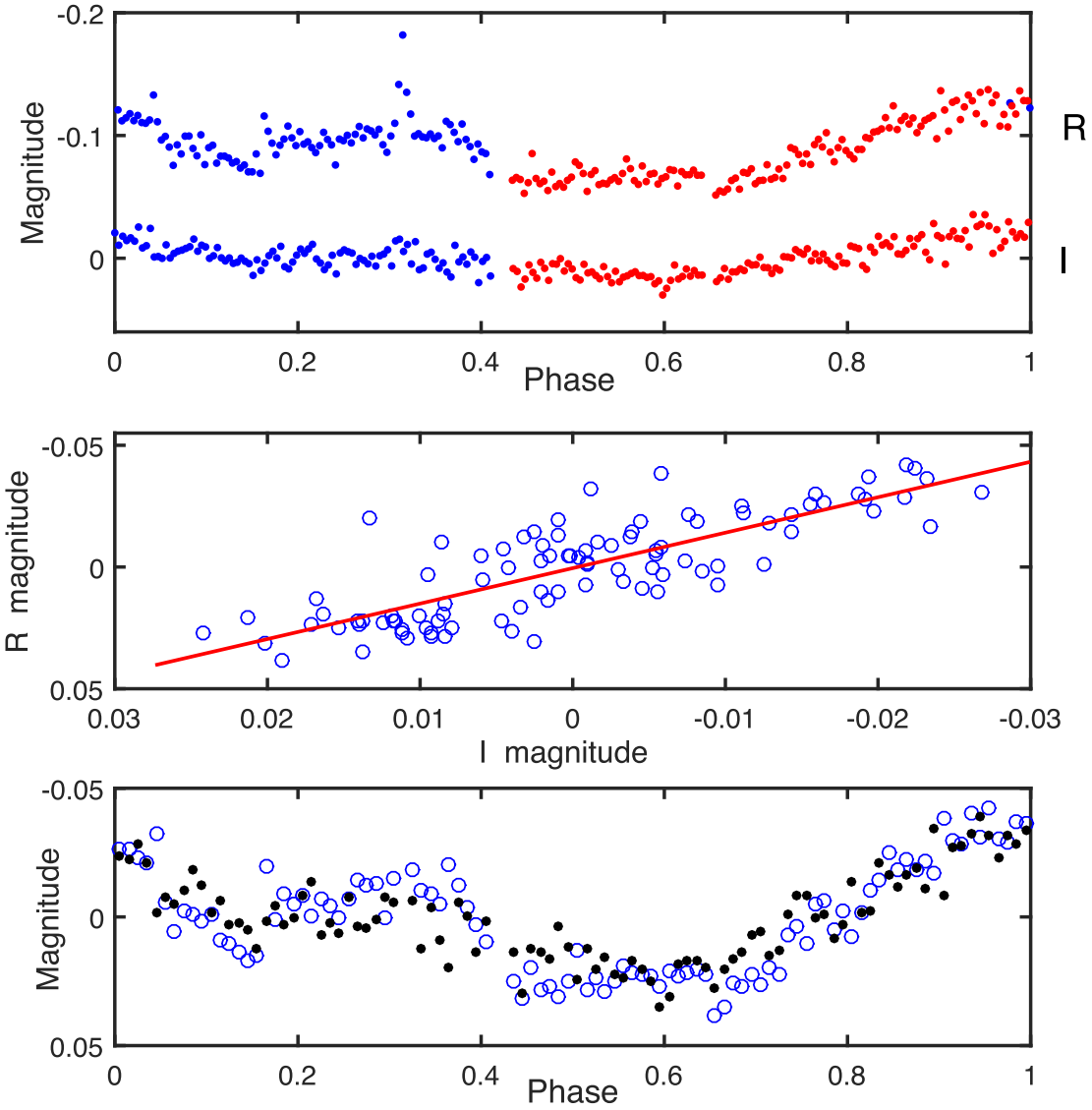

Figure 15. Top panel: Phase folded SAAO observations of J2323. The light-curve magnitude zero-points are arbitrary. Different coloured dots denote data from different nights. Middle panel: The relation between the *R* and *I* photometry, for J2323. The line is a linear regression fit. Magnitude zero-points are arbitrary. Bottom panel: Open circles denote the binned *R* phased light curve of J2323. The dots show scaled binned *I* filter photometry. The scale factor used is the slope of the line in the middle panel.

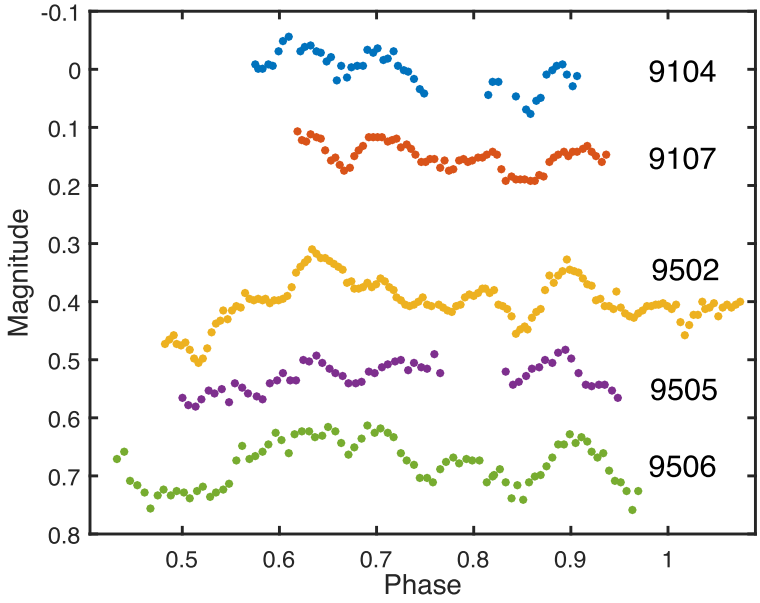

Figure 16. SAAO *I* filter photometry of J0021. Light curves are labelled with the last four digits of the Julian Day of observation. Observations on JD 2459107 and JD 2459505 have been, respectively, shifted by phases of −0.5 and +0.5 to facilitate comparison with data from other days. Magnitude zero-points of data from different nights are arbitrary.

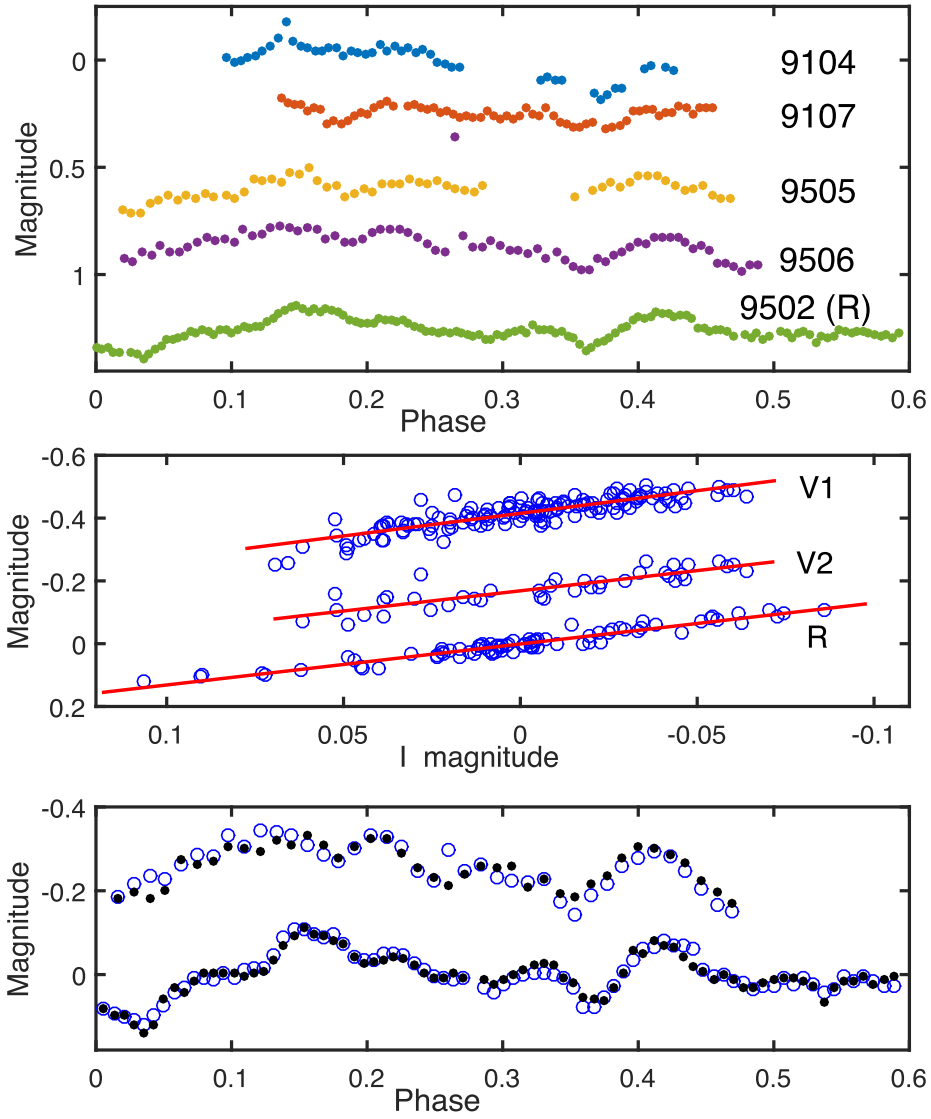

Figure 17. Top panel: SAAO *V* (top four light curves) and *R* (bottom light curve) photometry of J0021. Light curves are labelled with the last four digits of the Julian Day of observation. Observations on JD 2459107 and JD 2459505 have been, respectively, shifted by phases of −0.5 and +0.5 to facilitate comparison with data from other days. Magnitude zero-points of data from different nights are arbitrary. Note that the isolated point just below the JD 2459107 light curve is part of a flare on JD 2459506. Middle panel: The relation between *V* and *I*, and between *R* and *I* for J0021. Data marked '*V*1' include all *V* filter photometry, while '*V*2' are data from the most extended run (JD 2459506) only. The lines are linear regression fits. Magnitude zero-points are arbitrary. Bottom panel: Open circles denote binned *V* (top, JD 2459506) and *R* (bottom, JD 2459502) phased light curves of J0021. The dots show scaled binned *I* filter photometry. The scale factors used are the slopes of the lines in the middle panel.

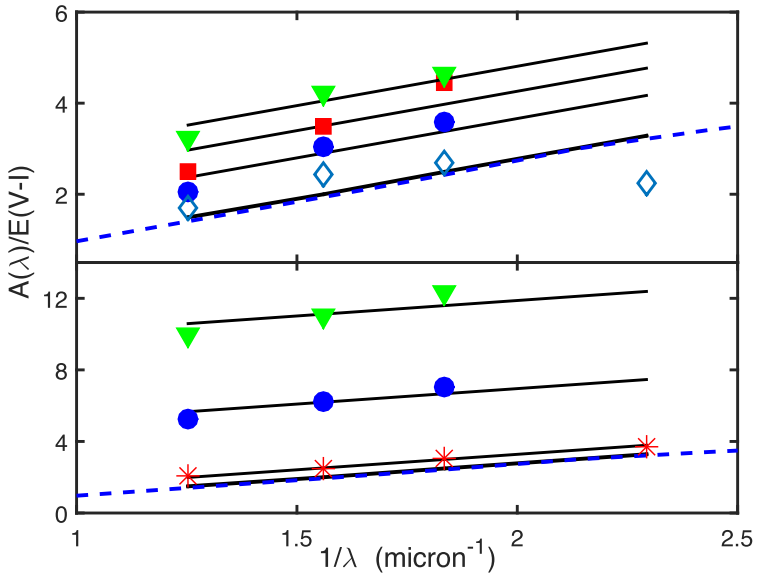

Figure 18. Amplitude scale factors a_λ [see equation (2)] converted to total-to-selective absorption ratios. Top panel: J2110 (blue circles), J1505 (red squares), J0021 (green triangles), J1252 (diamonds). Bottom panel: RIK 90 (red asterisks), J0113 (blue circles), J1601 (green triangles). The broken line lines connect extinction 'anchor points' (Fitzpatrick 1999, table 3), while solid lines overlapping the broken lines show the average Galactic extinction from Schlafly et al. (2016). Other solid lines are drawn parallel to the average Galactic extinction, in order to more clearly show that all but the RIK 90 data deviate from the slope of this relation.

DATA AVAILABILITY

SAAO photometry is available from the author of this paper; other observations are available from sources given in the paper.

REFERENCES

Ardila D., Martin E., Basri G., 2000, AJ, 120, 479
Bell C. P. M., Mamajek E. E., Naylor T., 2015, MNRAS, 454, 593
Bianchi L., Herald J., Efremova B., Girardi L., Zabot A., Marigo P., Conti A., Shiao B., 2011, Ap&SS, 335, 161
Bianchi L., Shiao B., Thilker D., 2017, ApJS, 230, 24
Chambers K. C. et al., 2016, preprint (arXiv:1612.05560)
Choi J., Dotter A., Conroy C., Cantiello M., Paxton B., Johnson B. D., 2016, ApJ, 823, 102
Cieza L. et al., 2007, ApJ, 667, 308
Cutri R. M. et al., 2014, Vizier Catalogue 2014yCat, 2328
De Marchi G. et al., 2016, MNRAS, 455, 4373
Donati J.-F. et al., 2014, MNRAS, 444, 3220
Fitzpatrick E. L., 1999, PASP, 111, 63
Froebrich D., Scholz A., Eislöffel J., Stecklum B., 2020, MNRAS, 497, 4602
Gagné J. et al., 2018, ApJ, 856, 23
Gaia Collaboration, 2021, A&A, 649, A1
Greaves J. S. et al., 2014, MNRAS, 438, L31
Günther M. N. et al., 2022, AJ, 163, 144
Henden A. A., Levine S., Terrell D., Welch D. L., 2015, AAS Meeting, 225, 336.16
Howell S. B. et al., 2014, PASP, 126, 398
Huang C. X. et al., 2020, RNAAS, 4, 204
Hughes A. M., Duchêne G., Matthews B. C., 2018, ARA&A, 56, 541
Jenkins J. M. et al., 2016, Proc SPIE, 9913, 99133E
Kirkpatrick J. D. et al., 2011, ApJS, 197, 19
Koen C., 2015, MNRAS, 450, 3991
Koen C., 2016, MNRAS, 463, 4383
Koen C., 2021a, MNRAS, 500, 1366
Koen C., 2021b, AJ, 162, 2
Koen C., 2022, MNRAS, 510, 1857
Kraus A. L., Shkolnik E. L., Allers K. N., Liu M. C., 2014, AJ, 147, 146
Luhman K. L., 2022, AJ, 163, 25
Martin D. C. et al., 2005, ApJ, 619, L1
Matthews B. C., Krivov A. V., Wyatt M. C., Bryden G., Eiroa C., 2014, in Henning T. K., Dullemond C. P., Klessen R. S., Beuther H., eds, Protostars and Planets VI. Univ. Arizona Press, Tucson, p. 521
Mendigutía I., Solano E., Vioque M., Balaguer-Nuñez L., Ribas A., Huélamo N., Rodrigo C., 2022, A&A, 664, A66
Morris B. M., Agol E., Davenport J. R. A., Hawley S. L., 2018, ApJ, 857, 39
Padgett D. L. et al., 2006, ApJ, 645, 1283
Pecaut M. J., Mamajek E. E., 2013, ApJS, 208, 9
Pecaut M. J., Mamajek E. E., 2016, MNRAS, 461, 794
Pecaut M. J., Mamajek E. E., Bubar E. J., 2012, ApJ, 756, 154
Riaz B., Gizis J. E., Harvin J., 2006, AJ, 132, 866
Rice J. B., Strassmeier K. G., Kopf M., 2011, ApJ, 728, 69
Ricker G. R. et al., 2015, JATIS, 1, 014003
Schlafly E. F. et al., 2016, ApJ, 821, 78
Schneider A. C., Shkolnik E. L., 2018, AJ, 155, 122
Skrutskie M. F. et al., 2006, AJ, 131, 1163
Stauffer J. et al., 2017, AJ, 153, 152
Stauffer J. et al., 2018, AJ, 155, 63
Stauffer J. et al., 2021, AJ, 161, 60
Voges W. et al., 1999, A&A, 349, 389
Walkowicz L. M., Hawley S. L., 2009, AJ, 137, 3297
Wolf C. et al., 2018, PASA, 35, E010
Zhan Z. et al., 2019, ApJ, 876, 127

This paper has been typeset from a TEX/LATEX file prepared by the author.